An investigation of compressible forced convection in a three dimensional tapered chimney by CUDA computation platform

Wu-Shung Fu *, Wei-Hsiang Wang, Yun Huang, Chung-Gang Li

Department of Mechanical Engineering, National Chiao Tung University, Hsinchu 30010, Taiwan, ROC

ARTICLE INFO

ABSTRACT

Compressible forced convection in a three dimensional tapered chimney is investigated numerically. Schemes of Roe and preconditioning are adopted to resolve compressible flow problem under a low speed velocity situation. Coordinates transformation of algebraic grid generation and non-reflecting boundary condition is used to execute the coordinated transformation of the tapered duct and decrease the computation domain, respectively. Computing procedures are performed on the CUDA computation platform which is developed recently and is a very effective tool. Due to the variation of the geometry of three dimensional tapered chimney, the flow velocity increases in the central region and decreases near the corner region. Therefore, heat transfer rates are enhanced remarkably in the central region and become inferior abruptly near the corner region. The efficiency of CUDA computation platform is marvelous, and the possibility of capability of super computation of individualization may be realized by using the CUDA computation platform.

1. Introduction

The chimney is a very important engineering equipment and indispensably used in high temperature systems of combustion, pollution control, ventilation, etc. The chimney is mainly composed of three parts of a large pedestal, a tapered duct and a small extending duct. Although the usage of the tapered duct causes flow problems in the chimney to become complicated, the importance of the practical application of the chimney is indisputable, and the study of heat transfer mechanisms in the chimney still receives a lot of attention.

About studies of heat transfer mechanisms in a convergent duct, in the past Sparrow et al. [1] first investigated natural convection in a two dimensional convergent channel experimentally and numerically, the convergent angles were 0°, 5°, 10° and 15°. The results showed that the larger the convergent angle was, the higher heat transfer rate could be gained and the trends were observed in both experimental and numerical studies. Furthermore, Sparrow et al. [2] extended the above study, and used the prediction of the maximum interwall spacing to calculate the Nusselt numbers of vertical parallel plates and proposed a correlation of Nusselt number, Rayleigh number and aspect ratio. Su and Lin [3] used the SIMPLEC method to calculate variations

of Nusselt number and pressure drop in a three dimensional conduct composing of two flat plates and two convergent plates. The convergent angles of 0°, 5°, 10° and 15° were adopted. The Nusselt number and pressure drop increased accompanying the increment of the convergent angle. Afterward Su and Lin [4] conducted an experimental work to validate the results obtained by the previous study. The results were similar to those of the previous study when the convergent angle increased. Kihm et al. [5] used Laser Specklegram Technique to investigate natural convection phenomena in a convergent duct. There five convergent angles and eight aspect ratios were considered to study the natural convection phenomena. The trends of experimental and theoretical results were similar. Mutama and Iacovides [6] conducted an experimental work to study thermal and velocity boundaries in a two dimensional long convergent duct with a small convergent angle. The results showed that because of the acceleration of the main flow the heat transfer rate of this model was prior to that of the parallel plates model. Said [7] used numerical simulation to investigate natural convection in a two dimensional convergent vertical channel. The results proposed an optimal correlation of the Nusselt number and variable parameters. Shalash et al. [8] performed numerical and experimental works to study the similar physical model used in [7]. At the low Rayleigh number, the Nusselt number increased with the increment of the convergent angle and vice versa. Bianco and Nardini [9] adopted the code of Fluent to investigate natural convection in two dimensional plates and observed a chocked flow to occur easily as the exit was very narrow. Bianco et al. [10] extended the pre-

Nomenclature

k	thermal conductivity (W/mK)
d_1	width of pedestal (m)
d_2	width of extending duct (m)
e	internal energy (J/kg)
l_1	length of pedestal (m)
l_2	length of tapered duct (m)
l_3	length of extending duct (m)
Nu_X	local Nusselt number defined in Eq. (30)
Nu_Y	local Nusselt number defined in Eq. (31)
$\overline{Nu}_{L_y}$	line average Nusselt number defined in Eq. (33)
$\overline{Nu}_A$	area average Nusselt number defined in Eq. (34)
P	pressure
Pr	Prandtl number
R	gas constant (J/kg/K)
Re	Reynolds number defined in Eq. (7)
t	time (s)
T	temperature (K)

T_0	temperature of surroundings (K)
T_h	temperature of heat surface (K)
u_0	velocity at inlet (m/s)
u, v, w	velocities in x, y and z directions (m/s)
U, V, W	dimensionless velocities in X, Y and Z directions
x, y, z	Cartesian coordinates (m)
X, Y, Z	dimensionless Cartesian coordinates

Greek symbols

γ	specific heat ratio
ϕ	tapered angle of chimney
ξ, η, ζ	curvilinear coordinates
θ	dimensionless temperature
μ	viscosity (N s/m^2)
μ_0	surrounding viscosity (N s/m^2)
ρ	density (kg/m^3)
ρ_0	surrounding density (kg/m^3)

vious study to investigate effects of different structures and parameters on the natural convection of the convergent channel. The results were applied to the range of the convergent angle lower than 10° and the Rayleigh number lower than 1.2×10^7. Furthermore, Bianco et al. [11] conducted an experimental work to observe flow variations by Laser sheet. The correlation among the Nusselt number, Rayleigh number and convergent angle were proposed. Kaiser et al. [12] used two codes of Fluent and Phoenics to study natural convection in a two dimensional convergent channel. The results were compared with those of the previous studies and the correlations among the Nusselt number, Rayleigh number, convergent angle and aspect ratio were proposed. Andreozzi et al. [13–15] investigated a series study of natural convection in convergent and divergent ducts. Effects of duct width and length on heat transfer rate were examined in detail.

Except the studies of natural convection in a convergent duct, Huang et al. [16] conducted an experimental work to investigate mixed convection in a two dimensional vertical convergent channel. A flow visualization skill was executed to observe the variations of flow structure and the relationships among the Nusselt number and related parameters were investigated. Gau et al. [17] used the physical model similar to the previous study [16] to study mixed convection in two dimensional horizontal parallel and convergent plates. The secondary flows and reasons of increment of Nusselt number were investigated. Gau and Liu [18] extended the previous study [17] to observe the structures of secondary flows in the convergent, divergent and parallel ducts. The eddy flow caused by the lateral unstability wave due to the heat surface set on the bottom surface was originally observed. The secondary flow occurred early in the divergent duct due to the deceleration effect that resulted in the heat transfer in the divergent duct being increased. Besides, Yang et al. [19] used a high turbulence intensity condition as an entrance condition to investigate the effect of a single inclined plate duct on a film-cooled mechanism experimentally. The results showed that under the small inclined angle range the film-cooled rate increased with the increment of the inclined angle and the turbulence intensity was advantageous to the film-cooled rate. Zamora and Kaiser [20] extended the previous study [12] and adopted the low Reynolds k–ε model matching different turbulence intensities as entrance conditions to investigate relationships among the flow rate and variable parameters from laminar to transient regions. The results could be applied to the Rayleigh number from 10^{-2} to 10^{12}, inclined angle from 0° to 30°, and convergent angle from 0° to 60°.

Besides, for unifying the shape of different ducts and facilitating computation processes, several methods of coordinates transformation were usually used to transfer the shape of convergent region to the same shape of the other regions. Tao et al. [21] used a method of body-fitted coordinate to investigate heat transfer mechanisms of a three dimensional wavy fin-and-tube heat exchanger. The increment of heat transfer rate was accompanying the increments of Reynolds number and number of wavy fin-and-tube. An optimal distance between fin plates was founded for obtaining better heat transfer rate. Castelloes et al. [22] adopted the generalized integral transform technique to transfer a two dimensional corrugated wavy channel. The results showed that heat transfer rate increased with the decrement of Peclet number and increment of the presence of corrupted walls. Wang and Chen [23,24] used the algebraic transformation method matching the cubic spline collocation and alternating-direction implicit methods to investigate a forced convection in a two dimensional wavy duct. The results showed that the increment of wave ratio and Reynolds number was advantageous to the heat transfer rate.

Furthermore, in order to save computing time in a three dimensional computation, parallel computational methods of OpenMP (Open Multi-Processing) and MPI (The Message Passing Interface) are usually used. However, it is difficult to profit both advantages of cost and computational efficiency of the above methods. Brandvik and Pullan [25] and Corrigan et al. [26] individually developed connecting and compiling programs to link a new computation platform of CUDA (Compute Unified Device Architecture) and to compute high speed compressible flow problems, respectively. From the point view of cost and computational efficiency, the results were remarkable and valuable. In the literature mentioned above, except [25] and [26], the fluid was regarded as an incompressible fluid.

The aim of the study investigates heat transfer mechanisms of compressible forced convection in a three dimensional tapered chimney numerically. Schemes of Roe [27], preconditioning [28] for resolving compressible flow under a low Mach number situation and MUSCL (Monotonic Upstream-Centered Scheme for Conservation Laws) [29] coordinating LUSGS (Lower-Upper Symmetric Gauss Seidel) [30] are adopted to resolve governing

equations. Methods of algebraic grid generation [31] and a non-reflecting boundary condition [32] are used to execute coordinates transformation and decrease the computational domain, respectively. Finally, computing procedures in which the related connecting and compiling processes are developed by ourselves are performed on the CUDA computation platform [33]. The results show that local Nusselt numbers near the central region of the tapered duct are enhanced remarkably due to the acceleration of flow speed caused by the decrement of cross section area. Oppositely, near the corner region of the tapered duct, the drag resistance of the fluid flow is increased and the flow speed is compulsorily decelerated which causes local Nusselt numbers to become inferior directly. As for the advantage of CUDA computational platform, the performance is marvelous.

2. Physical model

A three dimensional tapered chimney regarded as a physical model is shown in Fig. 1. Lengths of the pedestal, tapered duct and extending duct are l_1, l_2 and l_3, respectively. Widths of the pedestal and extending duct are d_1 and d_2, respectively. The tapered angle is ϕ and the cross section of the chimney is square. Fluids

with uniform velocity u_0 and temperature T_0 flow into the chimney at the inlet. The temperature of the surfaces of pedestal and tapered duct is constant and equal to T_h higher than T_0, and the surfaces of extending duct are adiabatic. The boundary condition of pressure at the outlet of the chimney is non-reflecting for saving the usage of computational grids. From a point view of application, the tapered angle is not larger than 45°. In order to extend the research range, four different tapered angles of 0°, 30°, 60° and 90° are selected.

For facilitating the analysis, the following assumptions are made:

1. The flow is laminar flow.
2. The work fluid is ideal gas and follows the equation of state of ideal gas.
3. The magnitudes of gradients of density and pressure on the whole surfaces in the normal direction are zero.

The governing equations are derived as follows:

$$\frac{\partial U}{\partial t} + \frac{\partial F_1}{\partial x} + \frac{\partial F_2}{\partial y} + \frac{\partial F_3}{\partial z} = 0 \tag{1}$$
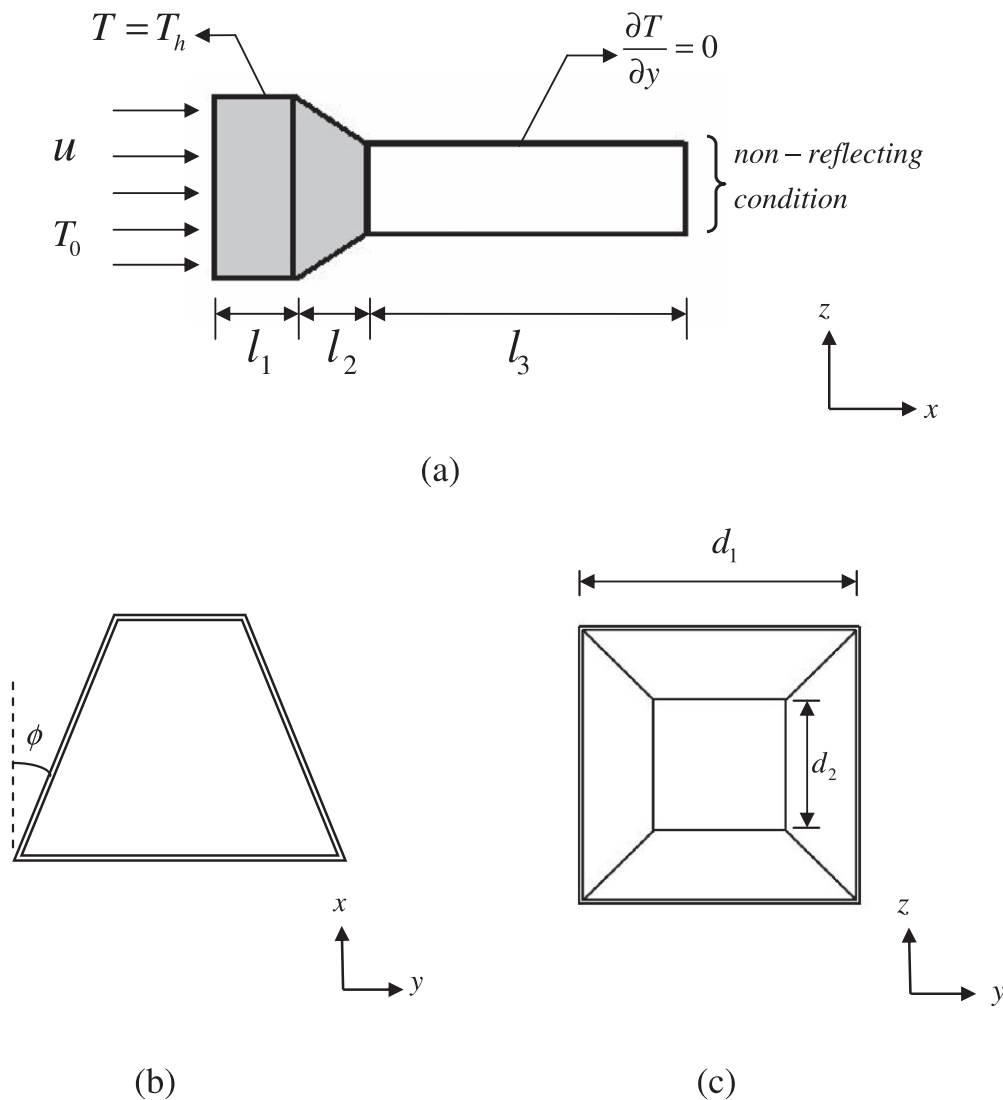

Fig. 1. Physical model.

The quantities included in U and F_i are separately shown in the following equations

$$U = \begin{pmatrix} \rho \\ \rho u \\ \rho v \\ \rho w \\ \rho e \end{pmatrix} \tag{2}$$

and

$$F_i = \begin{pmatrix} \rho u_i \\ \rho u_i u_1 + P\delta_{i1} - \mu A_{i1} \\ \rho u_i u_2 + P\delta_{i2} - \mu A_{i2} \\ \rho u_i u_3 + P\delta_{i3} - \mu A_{i3} \\ (\rho e + P)u_i - \mu A_{ij}u_j - k\frac{\partial T}{\partial x_i} \end{pmatrix}, \quad \forall i = 1,2,3 \tag{3}$$

where $u_1 = u$, $u_2 = v$, $u_3 = w$ and $A_{ij} = \frac{\partial u_j}{\partial x_i} + \frac{\partial u_j}{\partial x_i}$, the ideal gas equation is written by

$$P = \rho RT \tag{4}$$

The Sutherland's law is adopted to evaluate the viscosity and the thermal conductivity

$$\mu(T) = \mu_0 \left(\frac{T}{T_0}\right)^{\frac{2}{3}} \frac{T_0 + 110}{T + 110} \tag{5}$$

$$k(T) = \frac{\mu(T)\gamma R}{(\gamma - 1)Pr}$$

where

$\rho_0 = 1.1842 \text{ kg/m}^3$, $g = 9.81 \text{ m/s}^2$, $\mu_0 = 1.85 \times 10^{-5} \text{ N s/m}^2$, $T_0 = 298.0592 \text{ K}$, $\gamma = 1.4$, $R = 287 \text{ J/kg/K}$ and $Pr = 0.72$

To simplify the analysis, the following dimensionless variables are made

$$X = \frac{x}{d_1}, \quad Y = \frac{y}{d_1}, \quad Z = \frac{z}{d_1} \tag{6}$$
$$U = \frac{u}{u_0}, \quad V = \frac{v}{u_0}, \quad W = \frac{w}{u_0}$$

The compressibility and viscosity of the working fluid are considered, and the definition of the Reynolds number Re is defined as follows:

$$Re = \frac{\rho_0 u_0 d_1}{\mu_0} \tag{7}$$

3. Numerical method

Numerical methods of this study are mainly divided into four parts of numerical schemes, coordinates transformation, non-reflecting boundary condition and CUDA computation platform separately described as follows.

The Roe method [27] coordinating preconditioning method [28] are adopted to resolve the governing equations shown in Eq. (1). To derive Eq. (1), Eq. (8) can be obtained

$$\Gamma \frac{\partial U_p}{\partial t} + \frac{\partial F_1}{\partial x} + \frac{\partial F_2}{\partial y} + \frac{\partial F_3}{\partial z} = 0 \tag{8}$$

where Γ is a preconditioning matrix proposed by Weiss and Simth [28] and U_p is a primitive form of $[P, u, v, w, T]^t$.

To discretize Eq. (8), Eq. (9) is obtained. The terms of $\frac{\partial U_p}{\partial t}$ are differentiated by the second order backward difference, and the terms of $\frac{\partial F_1}{\partial x}$, $\frac{\partial F_2}{\partial y}$ and $\frac{\partial F_3}{\partial z}$ are differentiated by the central difference

$$\Gamma \frac{3U_p^{k+1} - 4U_p^k + U_p^{k-1}}{2\Delta t} + \frac{1}{\Delta x}\left(F_{1_{i+\frac{1}{2},j,k}}^k - F_{1_{i-\frac{1}{2},j,k}}^k\right)$$
$$+ \frac{1}{\Delta y}\left(F_{2_{i,j+\frac{1}{2},k}}^k - F_{2_{i,j-\frac{1}{2},k}}^k\right) + \frac{1}{\Delta z}\left(F_{3_{i,j,k+\frac{1}{2}}}^k - F_{3_{i,j,k-\frac{1}{2}}}^k\right) = 0 \tag{9}$$

Afterward the terms of U^{k+1} and F_i^{k+1} in Eq. (9) are necessary to be linearized and expressed as follows, respectively

$$U^{k+1} = U^k + M\Delta U_p \tag{10}$$

where $M = \frac{\partial U}{\partial U_p}$ and $\Delta U_p = U_p^{k+1} - U_p^k$

$$F_1^{K+1} = F_1^K + A_p \Delta U_p \tag{11}$$

where $A_p = \frac{\partial F_1^k}{\partial U_p}$ is the flux Jacobian and the same method is used for $B_p = \frac{\partial F_2^k}{\partial U_p}$ and $C_p = \frac{\partial F_3^k}{\partial U_p}$ in linearization of F_2^{K+1} and F_3^{K+1}, respectively.

To substitute Eqs. (10) and (11) into Eq. (9), the following equation is obtained

$$\Gamma \frac{3(U_p^k + M\Delta U_p) - 4U_p^k + U_p^{k-1}}{2\Delta t} + \delta_x(F_1^k + A_p\Delta U_p)$$
$$+ \delta_y(F_2^k + B_p\Delta U_p) + \delta_z(F_3^k + C_p\Delta U_p) = 0 \tag{12}$$

where δ_x, δ_y, and δ_z are central-difference operators.

Eq. (12) can be rearranged as the following form

$$\left[\Gamma M \frac{3}{2\Delta t} + (\delta_x A_p + \delta_y B_p + \delta_z C_p)\right]\Delta U_p = R^k \tag{13}$$

where $R^k = -\left(\frac{3U_p^k - 4U_p^k + U_p^{k-1}}{2\Delta t}\right) - (\delta_x F_1^k + \delta_y F_2^k + \delta_z F_3^k)$.

To divide the Γ in both sides, the following equation is obtained

$$\left[M\frac{3}{2\Delta t} + \Gamma^{-1}(\delta_x A_p^k + \delta_y B_p^k + \delta_z C_p^k)\right]\Delta U_p = \Gamma^{-1}R^k \tag{14}$$

The solver of Eq. (15) is the LUSGS implicit method proposed by Yoon and Jamesont [30]

$$A_p = \Gamma^{-1}A_p^k$$
$$B_p = \Gamma^{-1}B_p^k \tag{15}$$
$$B_p = \Gamma^{-1}C_p^k$$

As for the computation of $R^k = -\left(\frac{3U_p^k - 4U_p^k + U_p^{k-1}}{2\Delta t}\right) - (\delta_x F_1^k + \delta_y F_2^k + \delta_z F_3^k)$ in RHS (right hand side) of Eq. (10), the terms of F_i in Eq. (3) based on Cartesian coordinate can be divided into two parts. One is the inviscid term $F_{inviscid}$

$$F_{inviscid} = \begin{pmatrix} \rho u_i \\ \rho u_i u + P\delta_{i1} \\ \rho u_i v + P\delta_{i2} \\ \rho u_i w + P\delta_{i3} \\ (\rho e + P)u_i \end{pmatrix} \tag{16}$$

The other is viscous term $F_{viscous}$

$$F_{viscous} = -\begin{pmatrix} 0 \\ \mu A_{i1} \\ \mu A_{i2} \\ \mu A_{i3} \\ \mu A_{ij}u_j + \lambda\frac{\partial T}{\partial x_i} \end{pmatrix} \tag{17}$$

The upwind difference scheme developed by Roe [27] is employed in discretion of the term of $F_{inviscid}$ at the cells interface $(i + \frac{1}{2})$ and expressed as follows at a low Mach number situation

$$F_{inviscid,i+\frac{1}{2}} = \frac{1}{2}(F_R + F_L) - \frac{1}{2}\{|\Gamma^{-1}A_p|\Delta U_P\} \tag{18}$$

The third order MUSCL scheme proposed by Abalakin et al. [29] is used to compute Eq. (15).

The derivative terms of $A_{ij} = \frac{\partial u_j}{\partial x_i} + \frac{\partial u_j}{\partial x_i}$ in Eq. (14) are computed by the fourth order central difference

$$\frac{\partial u}{\partial x} = \frac{u_{i-2} - 8u_{i-1} + 8u_{i+1} - u_{i+2}}{12\Delta x} + o(\Delta x^4) \tag{19}$$

The advantage of usage of LUSGS implicit method is to improve efficiency.

On the adiabatic surface, the boundary conditions are

$$P(i,0,k) = P(i,1,k)$$
$$u(i,0,k) = -u(i,1,k)$$
$$v(i,0,k) = -v(i,1,k) \tag{20}$$
$$w(i,0,k) = -w(i,1,k)$$
$$T(i,0,k) = T(i,1,k)$$

$$P(i,j,0) = P(i,j,1)$$
$$u(i,j,0) = -u(i,j,1)$$
$$v(i,j,0) = -v(i,j,1) \tag{21}$$
$$w(i,j,0) = -w(i,j,1)$$
$$T(i,j,0) = T(i,j,1)$$

On the heat surface, the boundary conditions are

$$P(i,0,k) = P(i,1,k)$$
$$u(i,0,k) = -u(i,1,k)$$
$$v(i,0,k) = -v(i,1,k) \tag{22}$$
$$w(i,0,k) = -w(i,1,k)$$
$$T(i,0,k) = 2T_h - T(i,1,k)$$

where T_h is the wall temperature.

0 indicates the ghost cell and 1 indicates the cell closest to the wall.

As for the boundary conditions at the outlet, in order to avoid the flow in the channel polluted by the reflections of acoustic waves induced by the compressible flow, the non-reflecting boundary conditions are then necessarily used at the outlet of the chimney.

In a high speed compressible flow condition, the method of LODI (local one-dimensional inviscid relations) proposed by Poinsot and Lele [32] was suitably adopted for determining the non-reflecting boundary conditions at the outlet. However, a preconditioning matrix is not necessary in the above method that causes the method to be not adopted appropriately for determining the non-reflecting boundary conditions at the outlet under a low speed compressible flow. As a result, the method developed by Fu et al. [34] is necessary for resolving the non-reflection boundary conditions under a low speed compressible flow.

In order to execute computation procedures efficiently and conveniently, a coordinates transformation method of algebraic grid generation [31] is used to transfer from the physical to computational domain shown in Fig. 2, and the relationships of the variables of physical domain to those of the computational domain are expressed as follows, respectively.

$$\tau = t$$
$$\xi = \xi(t,x,y,z)$$
$$\eta = \eta(t,x,y,z) \tag{23}$$
$$\varsigma = \varsigma(t,x,y,z)$$

To use chain rule, the following equation can be derived

Physical domain

Computational domain

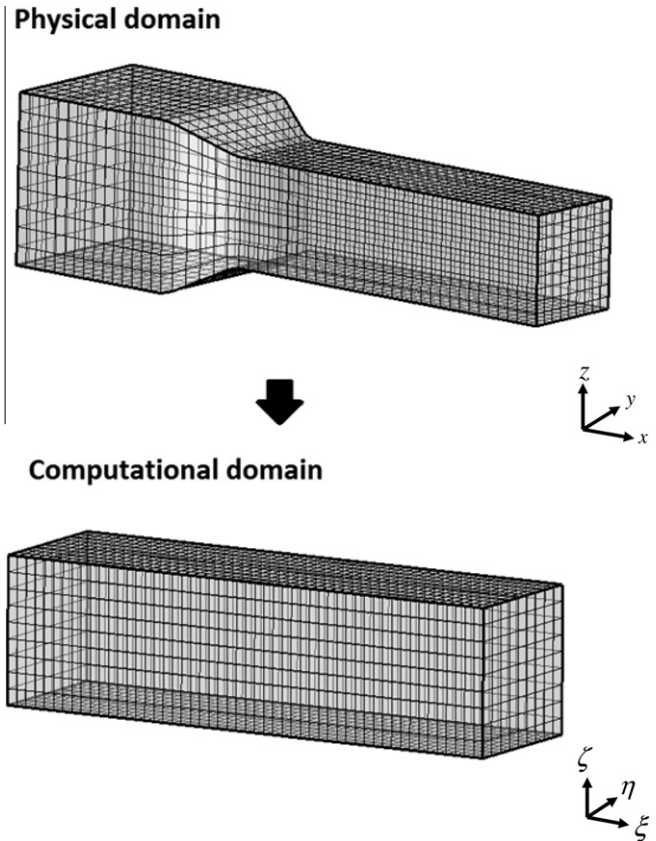**Fig. 2.** Diagram of the coordinates transformation.

$$\frac{\partial}{\partial t} = \frac{\partial}{\partial \tau} + \xi_t \frac{\partial}{\partial \xi} + \eta_t \frac{\partial}{\partial \eta} + \varsigma_t \frac{\partial}{\partial \varsigma}$$

$$\frac{\partial}{\partial x} = \xi_x \frac{\partial}{\partial \xi} + \eta_x \frac{\partial}{\partial \eta} + \varsigma_x \frac{\partial}{\partial \varsigma}$$

$$\frac{\partial}{\partial y} = \xi_y \frac{\partial}{\partial \xi} + \eta_y \frac{\partial}{\partial \eta} + \varsigma_y \frac{\partial}{\partial \varsigma} \tag{24}$$

$$\frac{\partial}{\partial z} = \xi_z \frac{\partial}{\partial \xi} + \eta_z \frac{\partial}{\partial \eta} + \varsigma_z \frac{\partial}{\partial \varsigma}$$

Between two domains, a Jacobian matrix is expressed as follows:

$$J = \frac{\partial(\xi, \eta, \varsigma)}{\partial(x, y, z)}$$
$$= \frac{1}{x_\xi(y_\eta z_\varsigma - y_\varsigma z_\eta) - x_\eta(y_\xi z_\varsigma - y_\varsigma z_\xi) + x_\varsigma(y_\xi z_\eta - y_\eta z_\xi)} \tag{25}$$

A quarter of tapered duct in the first quadrant can be transferred to a rectangular duct via the following equation

$$x = \xi$$

$$y = \left(\frac{d_1}{2} + \frac{\frac{d_2}{2} - \frac{d_1}{2}}{l_2}\xi\right)\eta \tag{26}$$

$$z = \left(\frac{d_1}{2} + \frac{\frac{d_2}{2} - \frac{d_1}{2}}{l_2}\xi\right)\varsigma$$

To project Eq. (26) on the negative axis of y indicated in Eq. (27), the half tapered duct can be transferred into a corresponding rectangular duct

$$x = \xi$$
$$y = -\left(\frac{d_1}{2} + \frac{\frac{d_2}{2} - \frac{d_1}{2}}{l_2}\xi\right)\eta \tag{27}$$
$$z = \left(\frac{d_1}{2} + \frac{\frac{d_2}{2} - \frac{d_1}{2}}{l_2}\xi\right)\varsigma$$

Finally, to project Eq. (27) on the negative axis of z indicated in Eq. (28), the whole tapered duct can be transferred into a complete rectangular duct

$$x = \xi$$
$$y = \pm\left(\frac{d_1}{2} + \frac{\frac{d_2}{2} - \frac{d_1}{2}}{l_2}\xi\right)\eta \tag{28}$$
$$z = -\left(\frac{d_1}{2} + \frac{\frac{d_2}{2} - \frac{d_1}{2}}{l_2}\xi\right)\varsigma$$

The main function of CUDA computation platform [33] which is a kind of integrated skill and developed by NVIDIA company is to integrate the performance of GPU (Graphics Processing Unit) arrayed in a video card installed in a host computer to a numerical parallel computation processor executed in the host computer.

Fig. 5. Comparison of numerical results with analytical solution [31] ($Re = 200$, $\phi = 0$).

Fig. 3. A brief structure of CUDA computation platform.

Fig. 6. Comparison of local Nusselt numbers of non-reflecting with fully developed conditions of heat surface along the centerline of streamwise direction ($Re = 200$, $\phi = 0$).
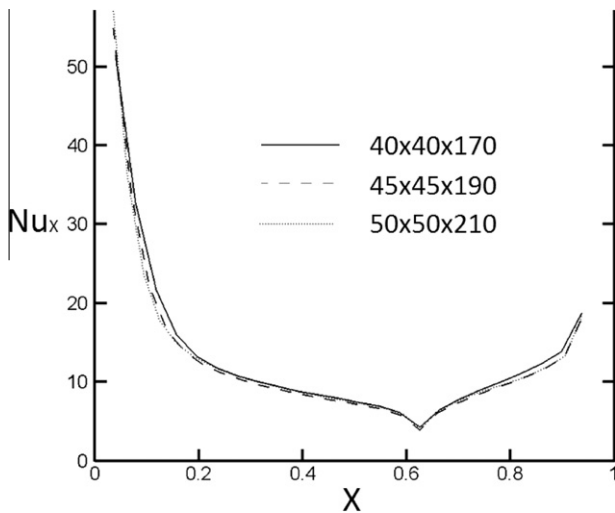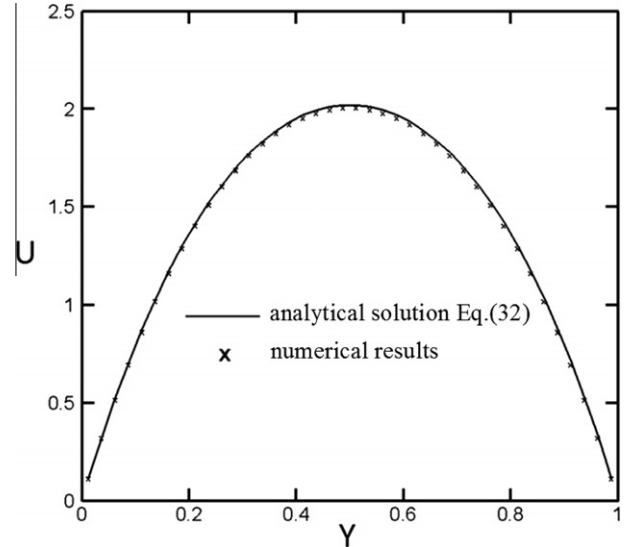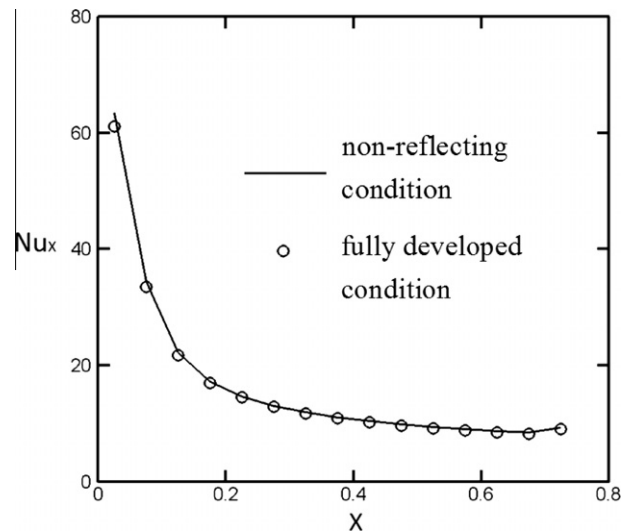

Fig. 4. Comparison of local Nusselt numbers of heat surface along the centerline of streamwise direction ($Re = 200$, $\phi = \frac{\pi}{6}$).

Table 1
Comparison of computing efficiency.

Type	CPU Intel Quad Q6600 (4 core)	CPU Intel Core i7 (4 core)	GPU Nvidia Tesla C1060
Grids	$190 \times 45 \times 45$	$190 \times 45 \times 45$	$190 \times 45 \times 45$
Parallel method	OpenMp	OpenMp	CUDA
s/step	0.93	0.494	0.197
Scaling	1	1.88	4.72

A very large quantity (usually several hundreds) of stream processors of which the main function is to execute computation are included in GPU, then it is very appropriate to perform parallel computation via exclusive connecting and compiling processes developed by users linking to the CUDA computation platform and host computer. A brief indication of the CUDA structure coordinating the host computer is shown in Fig. 3. A program according to compiling sequence is alternately executed in the host which includes CPU and memory, and device which is the main part of the CUDA computation platform including GPU and memory, respectively. Programs executed in the host and the device are called as serial code and kernel, respectively. Threads are the basic echelon of structure and grouped into a block, several blocks form the grid as an executing array in the kernel.

When the program is executed in the kernel by turns, the program distributed in necessary quantities of blocks and threads is mainly based on the demand of memory for computing procedures of parallel computation. One instruction is arrayed in one thread which is executed by a stream processor. As the stage of parallel computation executed in the kernel is finished, the results are sequentially collected and integrated with other results obtained by previous stages in the program. A next stage of the parallel computation begins to be executed continuously.

A procedure calculating the equations mentioned above is briefly described as follows:

(1) Assign the inlet conditions of pressure, velocities and temperatures.
(2) Use MUSCL method to calculate Eq. (14) to obtain the magnitude of ΔU_p.
(3) Substitute the magnitude of ΔU_p into Eq. (18) and use Roe method to calculate the magnitudes of inviscid terms of $F_{inviscid}$.
(4) Calculate Eq. (19) to obtain the magnitudes of viscous terms and substitute in Eq. (17).
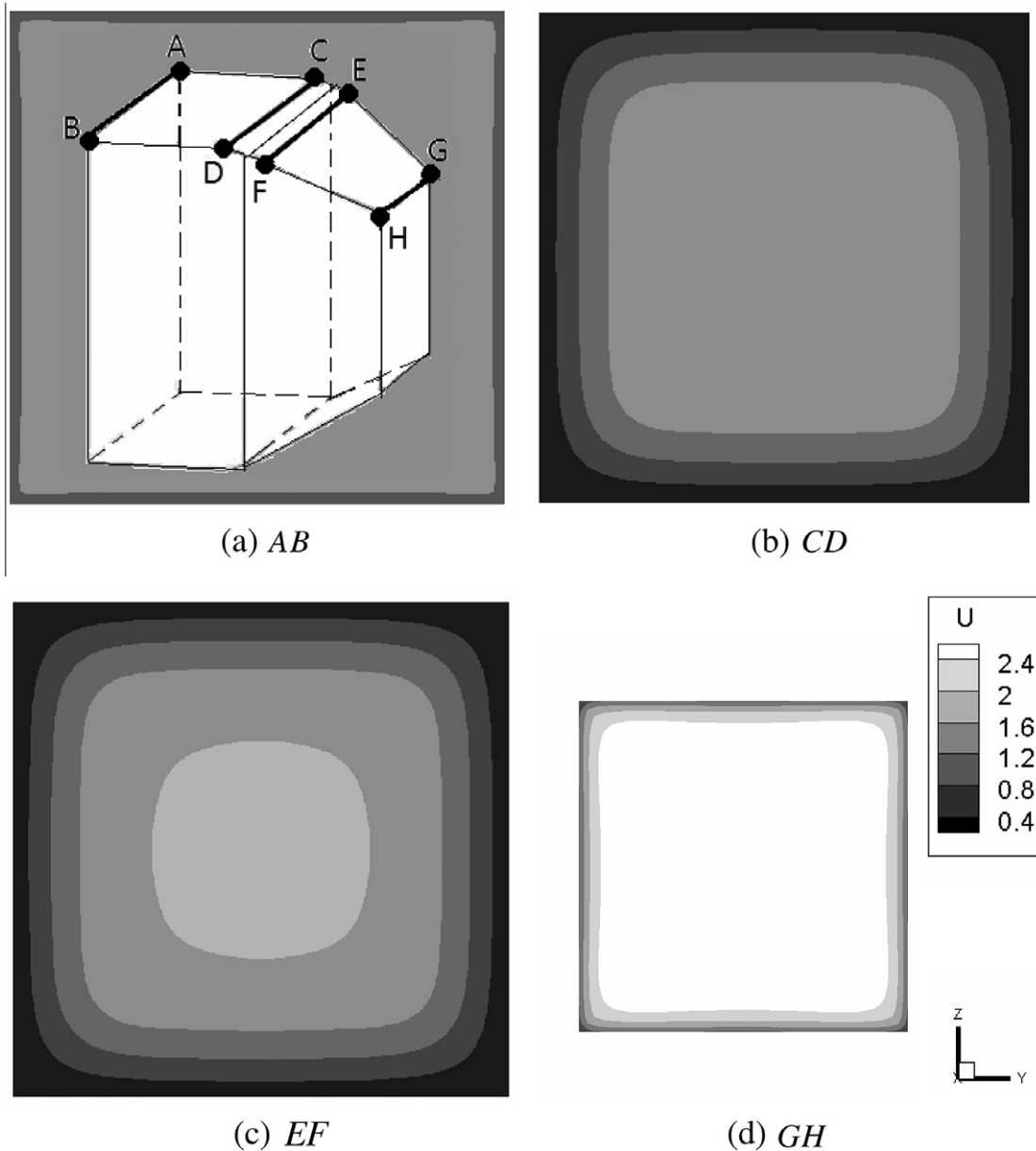(5) Solve U_p^{k+1}.

(a) AB

(b) CD

(c) EF

(d) GH

Fig. 7. Distributions of velocity U on AB, CD, EF and GH cross sections ($Re = 200$, $\phi = \frac{\pi}{6}$).

$$U_p^{k+1} = U_p^k + \Delta U_p^k \tag{29}$$

(6) Calculate Eq. (9) and examine the convergence of the iterational computation of U_p^{k+1}. Repeat (2)–(5) until $\frac{U_p^{k+1} - U_p^k}{\Delta \tau} < \varepsilon$, $\varepsilon = 10^{-3}$.

4. Results and discussion

In this study, the ranges of four different tapered angles and two different Reynolds numbers are performed. Local Nusselt numbers along x and y axes are defined as follows, respectively

$$Nu_X = \frac{d_1}{k_0(T_h - T_0)}\left[k(T)\frac{\partial T}{\partial n}\right] \tag{30}$$

$$Nu_Y = \frac{d_1}{k_0(T_h - T_0)}\left[k(T)\frac{\partial T}{\partial n}\right] \tag{31}$$

where n is normal direction of the surface.

Grid distributions of $40 \times 40 \times 170$, $45 \times 45 \times 190$ and $50 \times 50 \times 210$ in x, y and z directions are tested to decide the appropriate grid distribution. From the results of local Nusselt numbers shown in Fig. 4, the grid distribution of $45 \times 45 \times 190$ is adopted. Comparison of the analytic solution [35] indicated by Eq. (32) and numerical results of this study at the outlet under a fully developed situation is shown in Fig. 5. Both results are well consistent

$$u(y,z) = \frac{4d_1^2}{\mu\pi^3}\left(-\frac{dp}{dx}\right)\sum_{i=1,3,5,\dots}^{\infty}(-1)^{\frac{(i-1)}{2}}\left[1 - \frac{\cosh\left(\frac{i\pi z}{d_1}\right)}{\cosh\left(\frac{i\pi}{2d_1}\right)}\right] \times \frac{\cos\left(\frac{i\pi y}{d_1}\right)}{i^3} \tag{32}$$

In Fig. 6, the results of local Nusselt numbers along the center line of xy plane separately obtained by the non-reflecting and fully developed conditions are compared. The accuracy of usage of non-reflecting conditions at the outlet is validated. Performance tests of CUDA computation platform are tabulated in Table 1 and the results are remarkable.

Shown in Fig. 7(a), there is a velocity distribution of U on the AB cross section. The darker the color is, the slower velocity is indicated. Near the inlet of the chimney, the effect of wall boundary on the velocity distribution appears first on the region neighboring the wall. Velocities of the other region are almost equivalent. In Fig. 7(b), a velocity distribution of U on the CD cross section away from the inlet is indicated. According to the shades of color, the formation of different velocity layers is observed clearly. Around the corner of the cross section, flowing fluids are restrained by both side walls of an angle that causes the slow velocity region to be apparent and larger than other regions away from the corner. This phenomenon is very disadvantageous to the heat transfer mechanism. In Fig. 7(c), a velocity distribution of U on the EF cross section near the inlet of the tapered duct is shown. The effect of contraction of the tapered duct on the velocity distribution appears, then the variation of shades of color on this cross section becomes remarkable. Velocities of flowing fluids accelerated in the central region are observed. Furthermore, in Fig. 7(d), a velocity distribution of U on the cross section GH at the outlet of tapered duct is shown. Due to the decrement of GH cross section area, flowing fluids in most regions are accelerated, and the drastic variation of shades of color indicating a narrow region close to the wall is observed that means the velocity boundary layer to be narrow and advantageous to the heat transfer mechanism. Around the corner region of cross section, the slow velocity region mentioned above still exists that causes the heat transfer rate in this region to be inferior.

Local Nusselt numbers distributed along y direction under a situation of $Re = 200$, $\phi = \frac{\pi}{6}$ are indicated in Fig. 8. The AB cross section is close to the inlet of chimney that results in local Nusselt numbers distributed on the $\overline{AB}$ line being larger than those distributed on other lines. Regions near both ends of the $\overline{AB}$ line are neighboring to the corner region mentioned above, then magnitudes of local Nusselt numbers in those regions get worse rapidly. The line $\overline{CD}$ is located on the downstream of the pedestal, and the velocity boundary layer shown in Fig. 7(b) becomes thick and has detriment of heat transfer mechanism. As a result, the magnitudes of local Nusselt numbers become small. Local Nusselt numbers on both ends of the line are still smaller than those on the central region. The $\overline{EF}$ line is located near the inlet of the tapered duct, the influence of the contraction of the tapered duct on fluid flows begins to appear shown in Fig. 7(c) that causes magnitudes of local Nusselt numbers on the $\overline{EF}$ line to be naturally superior to those on the $\overline{CD}$ line. Velocities of fluid flows are accelerated remarkably on the $\overline{GH}$ line due to the influence of the contraction of tapered duct that directly causes local Nusselt numbers on the $\overline{GH}$ line to
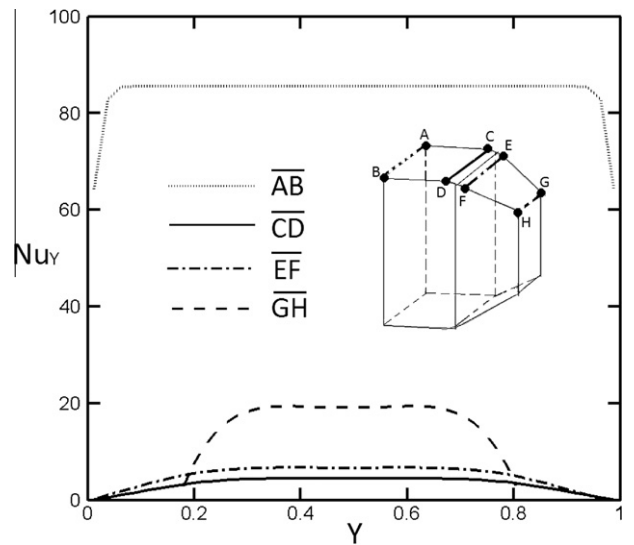
Fig. 8. Distributions of local Nusselt numbers on $\overline{AB}$, $\overline{CD}$, $\overline{EF}$ and $\overline{GH}$ lines ($Re = 200$, $\phi = \frac{\pi}{6}$).
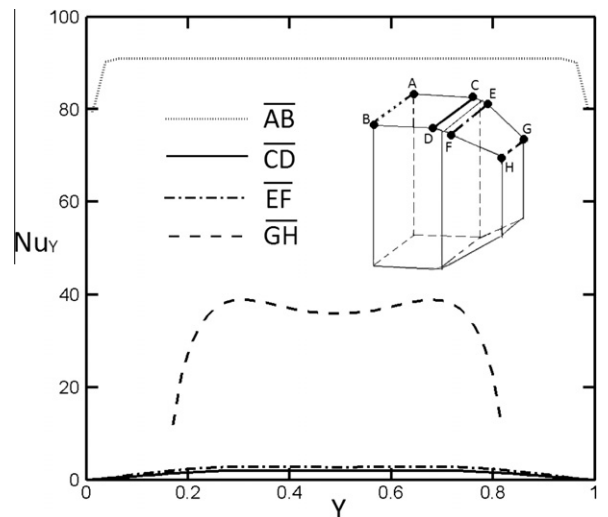
Fig. 9. Distributions of local Nusselt number on the $\overline{AB}$, $\overline{CD}$, $\overline{EF}$ and $\overline{GH}$ lines ($Re = 200$, $\phi = \frac{\pi}{3}$).

be enhanced. However, due to the drag effect induced by both sides of the angle near the corner region, the magnitudes of local Nusselt numbers decrease apparently.

Shown in Fig. 9, local Nusselt numbers distributed on lines of $\overline{AB}$, $\overline{CD}$, $\overline{EF}$ and $\overline{GH}$ are indicated, respectively, under a situation of $Re = 200$, $\phi = \frac{\pi}{3}$. Since the tapered angle ϕ of this situation is larger than that of the previous situation, the shape of the tapered duct becomes steeper, and the effect of the contraction of the tapered duct on fluid flows then become more apparent. Oppositely, the larger tapered angle causes the angle held between the pedestal and tapered duct to be small that results in fluid flows having difficulty to flow around the border of the pedestal and the tapered duct. For matching the variation of the tapered angle, the direction of fluid flows at the inlet are changed slightly to the interior that makes the magnitudes of local Nusselt numbers on the $\overline{AB}$ line of Fig. 9 to be slightly larger than those of Fig. 8. The magnitudes of local Nusselt numbers distributed on $\overline{CD}$ and $\overline{EF}$ lines of Fig. 9 are generally smaller than those of Fig. 8 because of the reason suggested above.

Since the area of cross section GH decreases drastically, the velocities of fluids near the central region are accelerated apparently that causes the magnitudes of local Nusselt numbers to be enhanced. Regions in both ends of $\overline{GH}$ line, the magnitudes of local Nusselt numbers are still decreased by the serious drag resistance induced by both sides of walls of angle.

In Fig. 10, local Nusselt numbers distributed on lines of $\overline{AB}$, $\overline{CD}$, $\overline{EF}$ and $\overline{GH}$ are indicated, respectively, under a situation of $Re = 200$, $\phi = \frac{\pi}{2}$. Since the tapered angle is $\frac{\pi}{2}$, and the shape is a kind of sudden contraction. This situation easily produces a strong resistance for fluid flows. As a result, local Nusselt numbers shown in Fig. 10 are all smaller than those correspondingly shown in the previous figures of Figs. 8 and 9.

In Fig. 11, the tapered angle ϕ is equal to 0, the chimney becomes a rectangular duct. Lines of $\overline{CD}$, $\overline{EF}$ and $\overline{GH}$ are located in the downstream region, local Nusselt numbers distributed on those lines are almost equivalent. Line AB is located at the inlet, naturally local Nusselt numbers are large and similar to those shown in the previous situations.
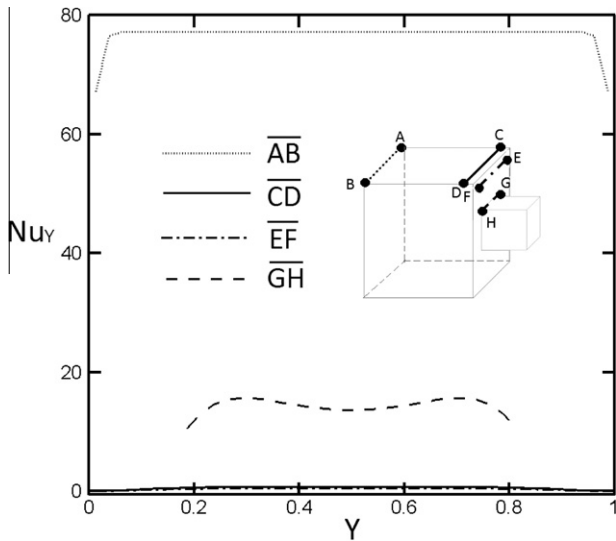

Fig. 10. Distributions of local Nusselt number on the $\overline{AB}$, $\overline{CD}$, $\overline{EF}$ and $\overline{GH}$ local Nusselt number ($Re = 200, \phi = \frac{\pi}{2}$).
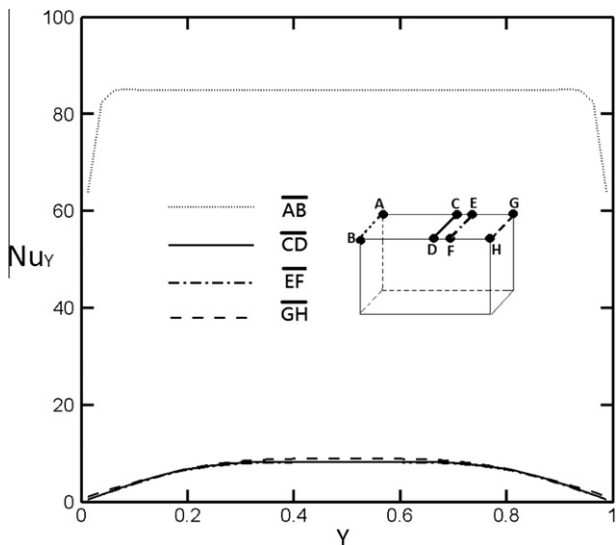

Fig. 11. Distributions of local Nusselt number on the $\overline{AB}$, $\overline{CD}$, $\overline{EF}$ and $\overline{GH}$ lines ($Re = 200$, $\phi = 0$).
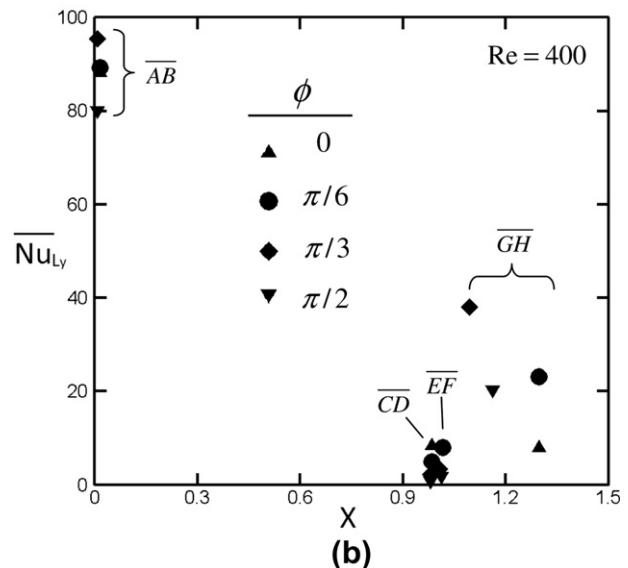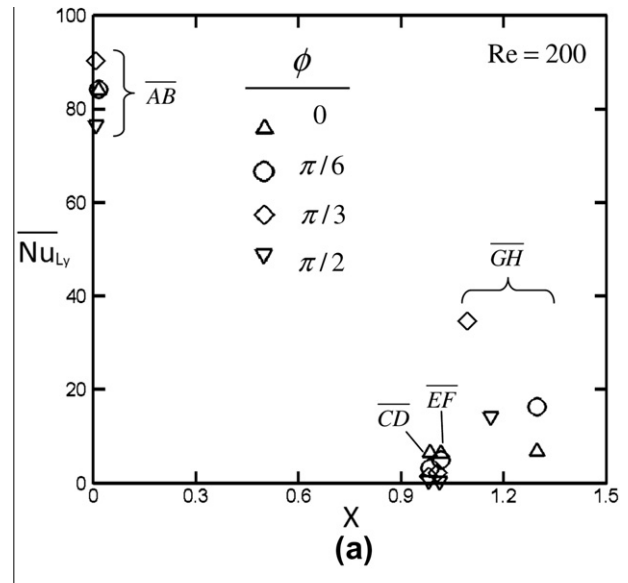

Fig. 12. Comparisons of average Nusselt numbers on the lines of $\overline{AB}$, $\overline{CD}$, $\overline{EF}$ and $\overline{GH}$ ($\phi = 0$, $\frac{\pi}{6}$, $\frac{\pi}{3}$ and $\frac{\pi}{2}$).

In Fig. 12, line average local Nusselt numbers distributed on lines of $\overline{AB}$, $\overline{CD}$, $\overline{EF}$ and $\overline{GH}$ are indicated under the whole situations, respectively. The line average local Nusselt number $\overline{Nu}_{L_y}$ is defined as follows:

$$\overline{Nu}_{L_y} = \frac{1}{L_y} \int_{L_y} Nu_y \, dy \quad (33)$$

Generally, the flow velocity directly affects the heat transfer mechanism, then the larger the Reynolds number is, the larger is the Nusselt number harvested. Since the effect of the tapered angle on the velocities of fluids accompanying the variation of location is different, and then the variations of the magnitudes of line average Nusselt numbers obtained by different angles in different lines are irregular.

Since the width of d_2 is assigned the same magnitude in the whole situations, the length of tapered duct l_2 is then changed according to the variation of tapered angle that causes the distance from the inlet to outlet of the tapered duct to be variable. Except $\phi = 0$ situation, the larger the tapered angle is, the shorter the distance mentioned above becomes. As a result, the variation of the cross section area of the tapered duct is drastic accompanying the increment of tapered angle. This phenomenon leads the region of the effect of the shape of the tapered duct on the velocities of fluids to be stretched out of the tapered duct and into the pedestal. As a result, except the region near the outlet of the tapered duct the magnitudes of the line average Nusselt number defined in Eq. (33) distributed on the heat surface in x axis of $\phi = \frac{\pi}{3}$ situation are smaller than those of $\phi = \frac{\pi}{6}$ situation show in Fig. 13.

Shown in Fig. 14, area average Nusselt numbers of different tapered angles are indicated. The area average Nusselt number $\overline{Nu}_A$ is defined as follows:

$$\overline{Nu}_A = \frac{1}{A} \int_{L_x} \int_{L_y} Nu_y \, dy \, dx \quad (34)$$

The area of heat surface is different accompanying the difference of the tapered angle mentioned above. In this study, the magnitude of area average Nusselt number of $\phi = \frac{\pi}{6}$ situation is superior to those of the other situations. This result is also consistent with the regular rule of the tapered angle being smaller than $\frac{\pi}{4}$ mentioned earlier.
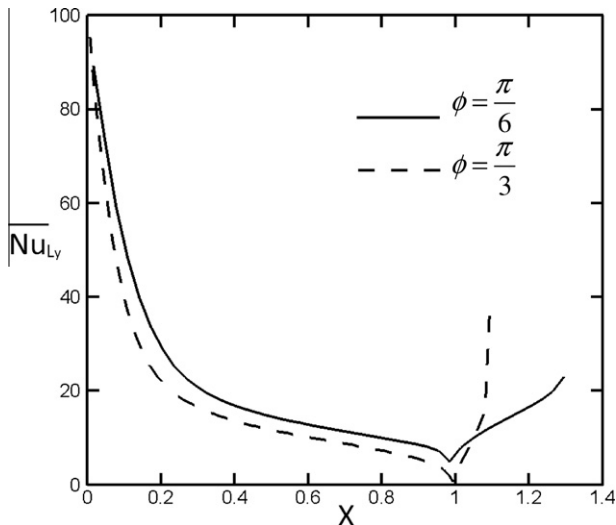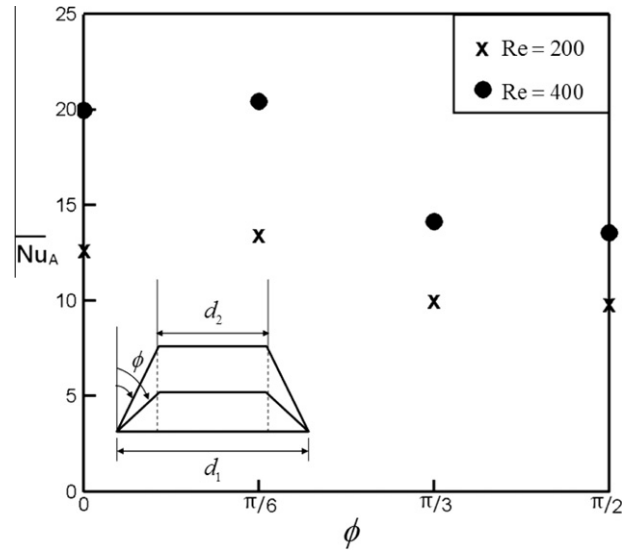

Fig. 14. Comparison of area average Nusselt numbers of $Re = 200$ with $Re = 400$ on heat surface.

5. Conclusions

An investigation of compressible forced convection in a three tapered chimney by CUDA computation platform is performed numerically. Several conclusions are drawn as follows:

(1) In this study, the optimal situation for heat transfer rate of forced convection is the condition of $\phi = \frac{\pi}{6}$.
(2) Local Nusselt numbers in the central region of tapered duct are enhanced due to the decrement of cross section area. Oppositely, local Nusselt numbers in the corner region of tapered duct are decreased due to the increment of drag resistance induced by both sides of angle.
(3) The CUDA computational platform has superiority for time-consuming computation processes.
(4) Super capability of computation of individualization can be realized by way of the CUDA computation platform.

Acknowledgements

Fig. 13. Comparison of line average Nusselt numbers of heat surface for $\phi = \frac{\pi}{6}$ and $\phi = \frac{\pi}{3}$ situations ($Re = 400$).

References

[1] E.M. Sparrow, R. Ruiz, Experiments on natural convection in divergent vertical channels and correlation of divergent, convergent, and parallel-channel Nusselt numbers, Int. J. Heat Mass Transfer 31 (1988) 2197–2205.
[2] E.M. Sparrow, R. Ruiz, L.F.A. Azevedo, Experimental and numerical investigation of natural convection in convergent vertical channel, Int. J. Heat Mass Transfer 31 (1988) 907–915.
[3] C.C. Su, H. Lin, Heat transfer and pressure drop characteristics of flow in convergent and divergent ducts, Int. J. Energy Res. 15 (1991) 7581–7591.
[4] C.C. Su, R.H. Lin, Experimental studies on flow in convergent and divergent ducts of rectangular cross section, Int. J. Energy Res. 21 (1997) 77–86.
[5] K.D. Kihm, J.H. Kim, L.S. Fletcher, Investigation of natural convection in heat transfer in converging channel flow using a Specklegram technique, J. Heat Transfer 115 (1993) 140–148.
[6] K.R. Mutama, H. Iacovides, The investigation of developing flow and heat transfer in a long converging duct, J. Heat Transfer 115 (1993) 897–903.
[7] S.A.M. Said, Investigation of natural convection in convergent vertical channels, Int. J. Energy Res. 20 (1996) 559–567.
[8] J.S. Shalash, J.D. Tarasuk, D. Naylor, Experimental and numerical studies of natural convection heat transfer in vertical converging channel flows,

proceeding of fourth experimental heat transfer, Fluid Mech. Thermodyn. (1997) 2167–2174.

[9] N. Bianco, S. Nardini, Numerical analysis of natural convection in air in a vertical convergent channel with uniformly heated conductive walls, Int. Commun. Heat Mass Transfer 32 (2005) 758–769.

[10] N. Bianco, L. Langellotto, O. Manca, S. Nardini, Thermal design and optimization of vertical convergent channels in natural convection, Appl. Thermal Eng. 26 (2006) 170–177.

[11] N. Bianco, O. Manca, S. Nardini, Experimental investigation on natural convection in a convergent channel with uniformly heated plates, Int. J. Heat Mass Transfer 50 (2007) 2772–2786.

[12] A.S. Kaiser, B. Zamora, A. Viedma, Correlation for Nusselt number in natural convection in vertical convergent channels at uniform wall temperature by a numerical investigation, Int. J. Heat Fluid Flow 25 (2004) 671–682.

[13] A. Andreozzi, B. Buonomo, O. Manca, Numerical study of natural convection in vertical channels with adiabatic extensions downstream, Numer. Heat Transfer A 47 (2005) 741–762.

[14] A. Andreozzi, B. Buonomo, O. Manca, Thermal management of a symmetrically heated channel–chimney system, Int. J. Thermal Sci. 48 (2009) 475–487.

[15] A. Andreozzi, B. Buonomo, O. Manca, Thermal and fluid dynamic behaviors in symmetrical heated channel–chimney systems, Int. J. Numer. Methods Heat Fluid Flow 20 (2010) 811–833.

[16] T.M. Huang, C. Gau, W. Aung, Mixed convection flow and heat transfer in a heated vertical convergent channel, Int. J. Heat Mass Transfer 38 (1995) 2445–2456.

[17] C. Gau, C.W. Liu, T.M. Huang, W. Aung, Secondary flow and enhancement of heat transfer in horizontal parallel-plate and convergent channels heating from below, Int. J. Heat Mass Transfer 42 (1999) 2629–2647.

[18] C. Gau, C.W. Liu, Onset of secondary flow and enhancement of heat transfer in horizontal convergent and divergent channels heated from below, Int. J. Heat Mass Transfer 47 (2004) 5427–5438.

[19] C.S. Yang, C.L. Lin, C. Gau, Film cooling performance and heat transfer over an inclined film-cooled surface at different convergent angles with respect to highly turbulent mainstream, Appl. Thermal Eng. 29 (2009) 167–177.

[20] B. Zamora, A.S. Kaiser, Optimum wall-to-wall spacing in solar chimney shaped channels in natural convection by numerical investigation, Appl. Thermal Eng. 29 (2009) 762–769.

[21] Y.B. Tao, Y.L. He, J. Huang, Z.G. Wu, W.Q. Tao, Three-dimensional numerical study of wavy fin-and-tube heat exchangers and field synergy principle analysis, Int. J. Heat Mass Transfer 50 (2007) 1163–1175.

[22] F.V. Castelloes, J.N.N. Quaresma, R.M. Cotta, Convective heat transfer enhancement in low Reynolds number flows with wavy walls, Int. J. Heat Mass Transfer 53 (2010) 2022–2034.

[23] C.C. Wang, C.K. Chen, Forced convection in a wavy-wall channel, Int. J. Heat Mass Transfer 45 (2002) 2587–2595.

[24] C.C. Wang, C.K. Chen, Mixed convection boundary layer flow of non-Newtonian fluids along vertical wavy plates, Int. J. Heat Fluid Flow 23 (2002) 831–839.

[25] T. Brandvik, G. Pullan, Acceleration of a 3D Euler solver using commodity graphics hardware, in: Forty-sixth AIAA Aerospace Sciences Meeting and Exhibit, AIAA, 2008.

[26] A. Corrigan, F.F. Camelli, R. Lohner, J. Wallin, Running unstructured grid-based CFD solvers on modern graphics hardware, Int. J. Numer. Methods Fluids 10 (2010), doi:10.1002/fld2254.

[27] P.L. Roe, Approximation Riemann solver, parameter vectors, and difference schemes, J. Comput. Phys. 43 (1981) 357–372.

[28] J.M. Weiss, W.A. Simth, Preconditioning applied to variable and constants density flows, AIAA 33 (1995) 2050–2056.

[29] I. Abalakin, A. Dervieux, T. Kozubskaya, A vertex centered high order MUSCL scheme applying to linearised Euler acoustics, INRIA 4459 (2002).

[30] S. Yoon, A. Jamesont, Lower–upper symmetric-Gauss–Seidel method for the Euler and Navier–Stokes equations, AIAA 26 (1988) 1025–1026.

[31] K.A. Hoffmann, S.T. Chiang, Computational Fluid Dynamics for Engineering, Engineering Education System, Wichita, Kan, 1993.

[32] T.J. Poinsot, S.K. Lele, Boundary conditions for Navier–Stokes, J. Comput. Phys. 101 (1992) 104–129.

[33] NVIDIA CUDA Compute Unified Architecture 3.0 programming Guide, NVIDIA Corporation, 2010.

[34] W.S. Fu, C.G. Li, C.P. Huang, J.C. Huang, An Investigation of a high temperature difference natural convection in a finite length channel without Boussinesq assumption, Int. J. Heat Mass Transfer 52 (2009) 2571–2580.

[35] F.M. White, Viscous Fluid Flow, McGrawHill Co., Ltd, 2006. p. 113.